PHYSICAL REVIEW A **80**, 033401 (2009)

One- and two-photon ionization cross sections of the laser-excited $6s6p\ ^1P_1$ state of barium

John R. Tolsma,[*] Daniel J. Haxton, and Chris H. Greene
Department of Physics and JILA, University of Colorado, Boulder, Colorado 80309-0440, USA

Rekishu Yamazaki and Daniel S. Elliott
Department of Physics and School of Electrical and Computer Engineering, Purdue University, West Lafayette, Indiana 47907, USA

(Received 6 June 2009; published 1 September 2009)

Stimulated by a recent measurement of coherent control in photoionization of atomic barium, we have calculated one- and two-photon ionization cross sections of the aligned $6s6p\ ^1P_1$ state of barium in the energy range between the $5d_{3/2}$ and $5d_{5/2}$ states of Ba^+. We have also measured these photoionization spectra in the same energy region, driving the one- or two-photon processes with the second or first harmonic of a tunable dye laser, respectively. Our calculations employ the eigenchannel R-matrix method and multichannel quantum defect theory to calculate the rich array of autoionizing resonances in this energy range. The nonresonant two-photon process is described using lowest-order perturbation theory for the photon-atom interactions, with a discretized intermediate-state one-electron continuum. The calculations provide an absolute normalization for the experiment, and they accurately reproduce the rich resonance structures in both the one- and two-photon cross sections, and confirm other aspects of the experimental observations. These results demonstrate the ability of these computationally inexpensive methods to reproduce experimental observables in one- and two-photon ionization of heavy alkaline earths, and they lay the groundwork for future studies of the phase-controlled interference between one- and two-photon ionization processes.

DOI: 10.1103/PhysRevA.80.033401 PACS number(s): 32.80.Fb, 32.80.Qk, 33.80.Rv, 32.80.Rm

I. INTRODUCTION

Through two-pathway coherent control of optical interactions, the outcome of a laser-driven interaction in an atom or molecule can be controlled by varying only the optical phase difference between various coherent laser fields [1–3]. Mutual phase coherence between the various optical fields and careful matching of optical wavefronts is required, but upon satisfaction of these conditions, various groups have used coherent control to modulate excitation rates of transitions [3,4], branching ratios of photodissociation [5,6], and even directional photocurrents in unbiased semiconductors [7,8]. When two or more dissociation channels are excited via interfering interactions, coherent control can be used to change the branching ratio into these different channels. Control is strongest when the transition amplitudes for the two pathways are of equal magnitude, and when the sinusoidal modulation of one product state and sinusoidal modulation of the other product state are π out of phase with one another. The latter condition leads to constructive interference for one product state under the conditions that yield destructive interference for the other. Thus, the observation by Gordon and co-workers [5,9] of a large phase difference between product states when photodissociating molecular $\mathrm{HI} \rightarrow \mathrm{HI}^+$ and $\mathrm{H}+\mathrm{I}^+$ was an important advance in the field.

The origin of the phase difference between product states generated significant interest [9–21], and ultimately channel mixing in the vicinity of discrete states embedded in the continuum (autoionizing or predissociating states) was identified as the dominant mechanism [9,11,12]. It is well-known from the scattering theory formulations, e.g., by Feshbach [22] and by Fano [23], that the wave-function components of the resonance and of the background can interfere quantum mechanically to alter the associated scattering observables, such as differential cross sections, alignment or orientation, or other quantities dependent on the phase of the scattered particles. Such interference occurs only when the operators labeling the wave-function components fail to commute with the observable of interest. The large phase-dependent variation in these observables is well-suited for the quantum control of the scattering, as well as other important applications such as the generation of cold molecules and degenerate quantum gases.

While there is qualitative support for the primary role that autoionizing or predissociating resonances play in modulating the phase difference between alternative pathways in coherent control experiments, there are no cases in which theory and experiment agree quantitatively, presumably because of the complexity of molecular systems for which these experiments and calculations have been carried out. For this reason, Yamazaki and Elliott [20,21] recently measured the phase shift in atomic barium, using the interference between one- and two-photon ionization of the aligned $6s6p\ ^1P_1$ state of barium in the energy range between the $5d_{3/2}$ and $5d_{5/2}$ states of Ba^+. Because the final states reached via the one- and two-photon processes are of opposite parity, the interference manifests itself as a modulation of the angular distribution of the photoelectrons, while the total cross sections are unaffected. In contrast to the usual photoelectron angular distribution experiments carried out where only a fixed number of electric dipole photons excite the observed final photoelectron energy [24,25], the angular distribution is modulated in the present case asymmetrically with regard to parity [1–3,26]. Observations of this modulation showed strong variations in the phase difference near several of the

---

[*] john.r.tolsma@gmail.com

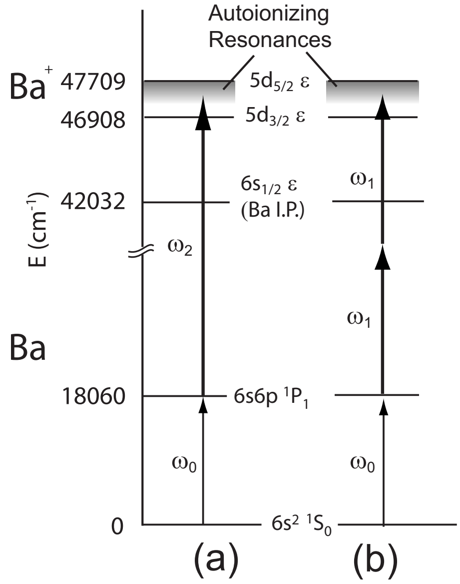

FIG. 1. An atomic barium energy-level diagram, showing the relevant energy levels and excitation schemes in our work. (a) The scheme for exciting the $6s6p\ ^1P_1$ intermediate state to the even-parity autoionizing resonances through the absorption of a single uv photon of wavelength $\lambda_2 \sim 343$ nm. (b) The scheme for accessing the odd continuum at the same final-state energy through two-photon absorption ($\lambda_1 \sim 685$ nm) from the same intermediate state is shown.

autoionizing resonances, with the largest phase shift of nearly 2π near the $5d\ ^2D_{5/2}15f_{3/2}$ two-photon peak at $47{,}216.5\ \text{cm}^{-1}$.

A calculation of these phase variations in the coherent control process requires an accurate description of the outgoing electronic waves, including their magnitudes and phases for various orbital angular momenta and spin orientations. This work reports a joint theoretical and experimental study of the cross sections for one- and two-photon ionization of atomic barium from the aligned $6s6p\ ^1P_1$ state. Determining these separate cross sections is a key prerequisite to an eventual description of the more sensitive phase interference effect. Following a discussion of the experimental measurements in Sec. II, we summarize our theoretical approach for calculating the spectra in Sec. III. Section IV compares the measured spectra with theory.

II. EXPERIMENT

Figure 1 presents an energy-level diagram with the relevant atomic states of barium and the experimental excitation schemes. Figure 1(a) shows the pathway leading to excitation of the even autoionizing resonances, while Fig. 1(b) displays the pathway to the odd-parity autoionizing resonances. In each case, the experiment first promotes ground-state ($6s^2\ ^1S_0$) barium to the $6s6p\ ^1P_1$ intermediate state by a linearly polarized laser beam at frequency ω_0, tuned near the resonance wavelength of approximately 553.7 nm. The subsequent absorption of two photons of the output of a second tunable dye laser at frequency ω_1 (wavelength λ_1 $\sim$685 nm), or of a single photon from the second harmonic of this field ω_2 (wavelength $\lambda_2 \sim 343$ nm) ionizes the atom to a continuum state between the $5d_{3/2}$ and $5d_{5/2}$ thresholds, 46,908.76 and $47{,}709.72\ \text{cm}^{-1}$ above the atomic ground state, respectively [27].

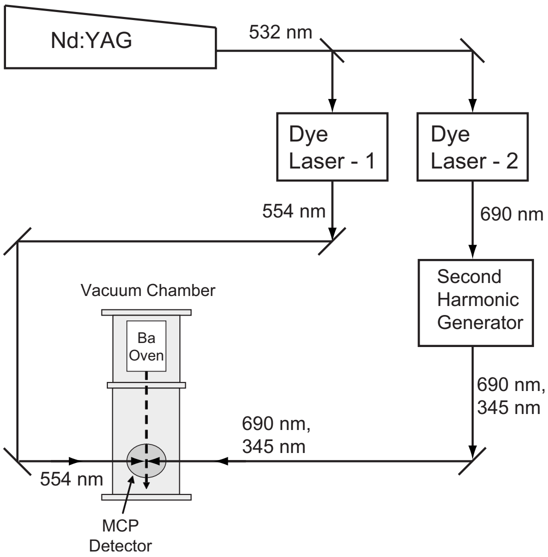

FIG. 2. The experimental setup. A Q-switched Nd:YAG laser pumps two tunable dye lasers, producing beams of wavelength 554 and $\sim$685 nm. The former prepares Ba in the $6s6p\ ^1P_1$ state, while the latter ionizes this state. The second-harmonic generator produces frequency-doubled light in the range 337–347 nm for single-photon ionization of the $6s6p\ ^1P_1$ state. The second-harmonic generator is omitted for measurement of the two-photon ionization spectra. The vacuum chamber contains the barium oven and microchannel plate (MCP) detector.

Because the excitation energy of the interaction reaches a final-state energy that exceeds the energy of the first-excited ($5d_{3/2}$) state of Ba^+, two states of the residual Ba^+ core can be populated. We distinguish these through measurements of the kinetic energies of the corresponding photoelectrons. Upon excitation of the $6s_{1/2}$ continuum channel, the photoelectron energy is approximately 0.6 eV, while the $5d_{3/2}$ channel correlates with the 0–0.1 eV electrons. We resolve the photoelectron energies using a microchannel plate detector assembly, described below. This detector also allows us to measure the photoelectron angular distributions, as described in Refs. [20,21].

A schematic of the experimental setup is depicted in Fig. 2. The second-harmonic output (532 nm) of a Q-switched Nd:YAG laser (10 Hz repetition rate) is used to pump two dye lasers, a homemade Littman-type laser (Dye Laser—1) with one longitudinally-pumped amplifier stage, and a Spectra Physics PDL-2 (Dye Laser—2). We use Rhodamine 590 dye in methanol in the first laser to generate the beam at frequency ω_0 (corresponding to a wavelength of 553.7 nm) and pulse energy 60 μJ. This laser is kept at a set wavelength during the experiment. To generate the laser beam at frequency ω_1, whose wavelength we vary in the range from 674–694 nm, we use LDS 698 dissolved in methanol in the PDL-2 laser. Scanning the wavelength of this laser allows us to tune across the continuum in the energy range between the

$5d_{3/2}$ and $5d_{5/2}$ thresholds. For the ultraviolet (uv) generation, the output of the PDL-2 is sent into a Type-I BBO nonlinear crystal, mounted on a motorized rotation stage controlled with the phase-matching servo system (Inrad Autotracker). The output of both lasers is in nearly a single longitudinal mode, and we set each of the laser polarizations to be horizontal before sending these beams into a vacuum chamber for the interaction with the atom beam. The pulse duration of each laser output is about 6 ns for ω_0 and 11 ns for ω_1. The wavelength of the PDL-2 output is controlled by a stepping motor attached to a grating inside the oscillator cavity, with a minimum step size of 0.0030 nm at 690 nm ($0.063\ \text{cm}^{-1}$). During a scan, we monitor the wavelength of the output of PDL-2 using a wavemeter with a specified frequency accuracy of $0.02\ \text{cm}^{-1}$ (Burleigh WA-4550). In practice, however, we observed inconsistencies in the wavelength readings of the wavemeter, which we attribute to degradation in the coatings of the wavemeter etalons, and we assign an uncertainty of 0.1 nm to the absolute wavelength reading ($2\ \text{cm}^{-1}$ in frequency). As we discuss later, we choose our absolute frequency calibration for the red two-photon spectrum as well as the uv one-photon spectrum using the known energy of the $6s7p\ ^1P_1$ bound state.

The first excitation laser-pulse ω_0 and the second excitation laser pulse (either at frequency ω_1 or ω_2) are sent into a vacuum chamber from opposite sides. The intensity peaks of the first and second excitation pulses coincide at the interaction region; the relative timing of the pulses is adjusted using a fast photodiode (with a resolution of 0.5 ns) and an optical delay. The pulse energy at ω_1 (ω_2) is 1.5 mJ (14 μJ). We weakly focus each of the laser beams into the interaction region to a beam radius of $w=300\ \mu\text{m}$, where w is the radius in which the intensity decreases by a factor e^{-2} from that of the peak value.

During a scan, we step the wavelength of the ω_1 beam with an increment of 0.012 nm. We limit the wavelength range of each scan to minimize the effect of pulse energy variations. The variations in the pulse energy of the 690-nm laser pulse are about 15%, while those of the uv pulses are about 20%. The overlap in adjacent scans is always sufficient to include at least one autoionizing resonance that is common to both, allowing us to piece the individual scans together to form the full scans. We adjust the amplitude of the individual scans slightly (on the order of 10%) to correct for differences in the laser-pulse energy. The two-photon spectra consist of 4 individual scans, while the uv spectra are composed of 8 individual scans.

The atomic barium beam is generated in an effusive oven inside the vacuum system. We maintain the temperature of the oven at 650 °C during the experiment. The atom beam generated from the oven is collimated using an aperture positioned before the interaction region. The diameter of the atomic beam at the interaction region is approximately 1 mm, with an estimated atom density of $4.3\times10^7\ \text{cm}^{-3}$. The background pressure around the interaction region is kept around 1×10^{-8} torr.

The photoelectrons from the interaction are collected using a microchannel plate (MCP) detector assembly [28]. The detailed explanation of the detector and the image processing for the product-resolved imaging can be found elsewhere [20,21,29] and we only discuss it briefly here. A pair of flat biased conducting meshes (81% transmitting) is constructed around the interaction region, which we use to generate a uniform dc electric field in the interaction region. The photoelectrons ejected by the barium atoms are accelerated toward the upper mesh by the bias field (~10 V/cm). The photoelectrons are amplified in the MCP, and each produces a pulse of light on the phosphor screen mounted behind. We image the phosphorescence from the phosphor screen using a charge-coupled device (CCD) camera interfaced to a laboratory PC through a framegrabber plug-in card, and accumulate and store the image for further image processing. We show an example of an image of the photoelectrons Fig. 3. The image collected can be resolved in kinetic energy and also provides the photoelectron angular distributions for each energy-resolved electron channel, as illustrated in the figure. We obtain the electron yield for each continuum channel by simply summing the electron counts in the image for the corresponding energy region. The typical number of electrons collected per laser pulse is about 10–150 electrons in a CCD region of 380×380 pixels. At every wavelength, we accumulate 100 images.

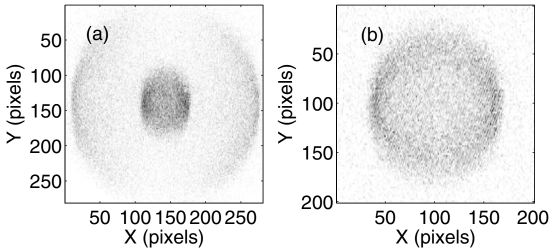

FIG. 3. An example of an image of the photoelectrons incident upon the MCP detector. In (a), the collecting field is ~11.4 V/cm, and we clearly see the image resolved by kinetic energy. The outer (inner) ring consists of photoelectrons that correlate to the $6s_{1/2}$ ($5d_{3/2}$) core state. In (b), the collecting field is reduced to ~2.9 V/cm in order to expand the $5d_{3/2}$ image. The laser polarization is oriented along the x axis.

The noise generated from the 554 and 685 nm laser pulse is less than 1 count/shot, while the noise from the uv probe, including the noise caused from the scattering of the uv pulse and the ionization of the background gas inside the vacuum system was about 13 counts/shot, uniformly distributed across the MCP detector.

We measured the $5d_{3/2}$ threshold energy of $46{,}890\ \text{cm}^{-1}$, differing by $18\ \text{cm}^{-1}$ from the value of Ref. [27]. This difference may be due to ac Stark shifts by the laser pulses, field ionization by the 10 V/cm dc collection field, or false counting of electrons with low kinetic energies. As the photoelectron kinetic energy decreases, the image radius becomes smaller and images of neighboring electrons start to overlap. False counting can occur for either extremely large electron numbers in the image and/or small kinetic energy of the electrons.

III. THEORY

We use atomic units throughout this section, unless otherwise specified.

Multichannel quantum defect theory (MQDT) [30,31] is well-established as an effective method to calculate photoionization spectra of atoms. The combination of MQDT and the R-matrix method [32] has been used to calculate rates of photoionization and electron-scattering processes for atoms and molecules. In particular, much attention has been given [33–44] to the problem of calculating the photoionization spectra of alkali earth atoms. We follow the methodology of these papers. In particular, we use a two-active-electron treatment of the barium atom, accounting for the [Xe] core using a model potential [33] with spin-orbit terms. For a complete review of the techniques employed in this work, see Ref. [44].

The initial states (denoted $|\Psi_0\rangle$) and intermediate states for the two photon calculation (denoted $|\epsilon\rangle$) are obtained from configuration-interaction (CI) calculations, and the final states (denoted $|\Psi_f\rangle$) are calculated using the eigenchannel R-matrix framework [45]. We employ partial waves up to and including $l=4$ in the single-particle basis. Our basis includes orbitals that obey a zero boundary condition at the R-matrix radius, which are used for all states, and orbitals that are nonzero on the boundary, used only in the final states. These orbitals are termed "closed-type" and "open-type," respectively. Those configurations with no open orbitals are denoted "closed" and those with one open orbital are denoted "open." Configurations are chosen according to their single-particle principal quantum numbers. We select configurations by restricting the highest value of the single-particle principal quantum number included to lie below a specified value, and by restricting the highest value that both single-particle principal quantum numbers may simultaneously exceed to a lower value, in both cases irrespective of l. Because we use a finite box size and a discretized continuum, the higher principal quantum number orbitals are not Rydberg orbitals but discretized box states, and by principal quantum number we mean the number of nodes plus l plus one.

The pseudopotential we employ [33] does not exactly reproduce the experimental energies. It is optimized to most accurately reproduce the ionization energies of Ba$^+$ and performs less well in reproducing the neutral energies. In some studies this has been improved by incorporation of a dielectronic polarization term in the Hamiltonian, but this has not been done here. Instead, we adjust the energy of the initial state (for both calculations) and a few of the experimentally probed intermediate states (for the two photon calculation). We list these adjustments in Table I. We also fix the channel thresholds, but these adjustments are smaller: by +0.73, −4.5, and +3.8 cm^{-1} for the $6s_{1/2}$, $5d_{3/2}$, and $5d_{5/2}$ channels.

A. One-photon calculations

The one-photon calculations precisely follow the methodology of, for instance, Ref. [38]. For these calculations we employ a R-matrix box size of $28a_0$. We employ MQDT to enforce the boundary condition for the wave function in the closed $5d_{5/2}$ channel, and also the higher $6p_{1/2}$ and $6p_{3/2}$ channels. Thus, these channels are "weakly closed" in MQDT terminology, and the exponentially decaying wave functions in these channels may have a nonzero value at the R-matrix boundary. Higher channels are strongly closed and obey a zero boundary condition there.

TABLE I. Initial and intermediate states whose energies are fixed in the calculations to the experimental values listed.

State	J	Experimental energy (cm^{-1})	Energy adjustment (experimental–calculated)
$^1P_1$ ($6s6p$) [a]	1	18060.261	−208.80
^3D ($5d7s$) [b]	1	32805.169	−34.79
^3D ($5d7s$) [c]	2	32943.774	−20.54
^1D ($5d7s$) [c]	2	33796.011	22.77
^3S ($6s8s$) [c]	1	33905.358	47.92

[a] Initial state.
[b] Intermediate-state resonance visible in two-photon calculation.
[c] Other intermediate states used in two-photon calculation.

For the one-photon calculation, our configuration list includes closed configurations in which the lowest principal quantum number is no greater than nine (e.g., the $6s$ through the $9s$), and in which the highest principal quantum number is no greater than 15 and 23 for the initial and final states, respectively. This gives 704 configurations for the initial state and 594, 1454, and 1998 configurations for final states with $J=0$, 1, and 2, respectively.

B. Two-photon calculations

Two-photon atomic ionization has been treated theoretically by several methods. A recent R-matrix Floquet treatment is described in Ref. [46]. Some calculations [47–51] have utilized the R-matrix-plus-MQDT-based descriptions of two-photon ionization in light alkaline earths, e.g., magnesium and calcium, as in the present work on the heavier barium atom. Two-color two-photon ionization of barium was treated using a combination of the R-matrix method, MQDT, and the Feshbach projection operator formalism [22], within an adiabatic Floquet model, in Ref. [52]. An L^2 method employing an integral equation for the K matrix was used in Ref. [53].

The two-photon ionization amplitude in second-order perturbation theory for the radiation-matter interaction can be defined

$$T_{f0}(\omega) = \lim_{\eta\to 0^+}\int d\varepsilon \frac{\langle\Psi_f|\vec{D}\cdot\hat{e}|\varepsilon\rangle\langle\varepsilon|\vec{D}\cdot\hat{e}|\Psi_0\rangle}{(E_0+\omega-\varepsilon-i\eta)}. \qquad (1)$$

The integration in this equation is meant to include a summation over bound states and an integration over continuum states. When above-threshold ionization (ATI) is energetically forbidden, the outgoing wave boundary condition in Eq. (1) can be replaced by a standing-wave boundary condition. This approximation, combined with a discretization of the continuum, is the strategy adopted here and in, for example, Refs. [49–51,54]. In Ref. [54] an extrapolation procedure was used to obtain spectra in the ATI energy range; in its most straightforward application, however, a treatment using discretized standing-wave continuum states is inappro-

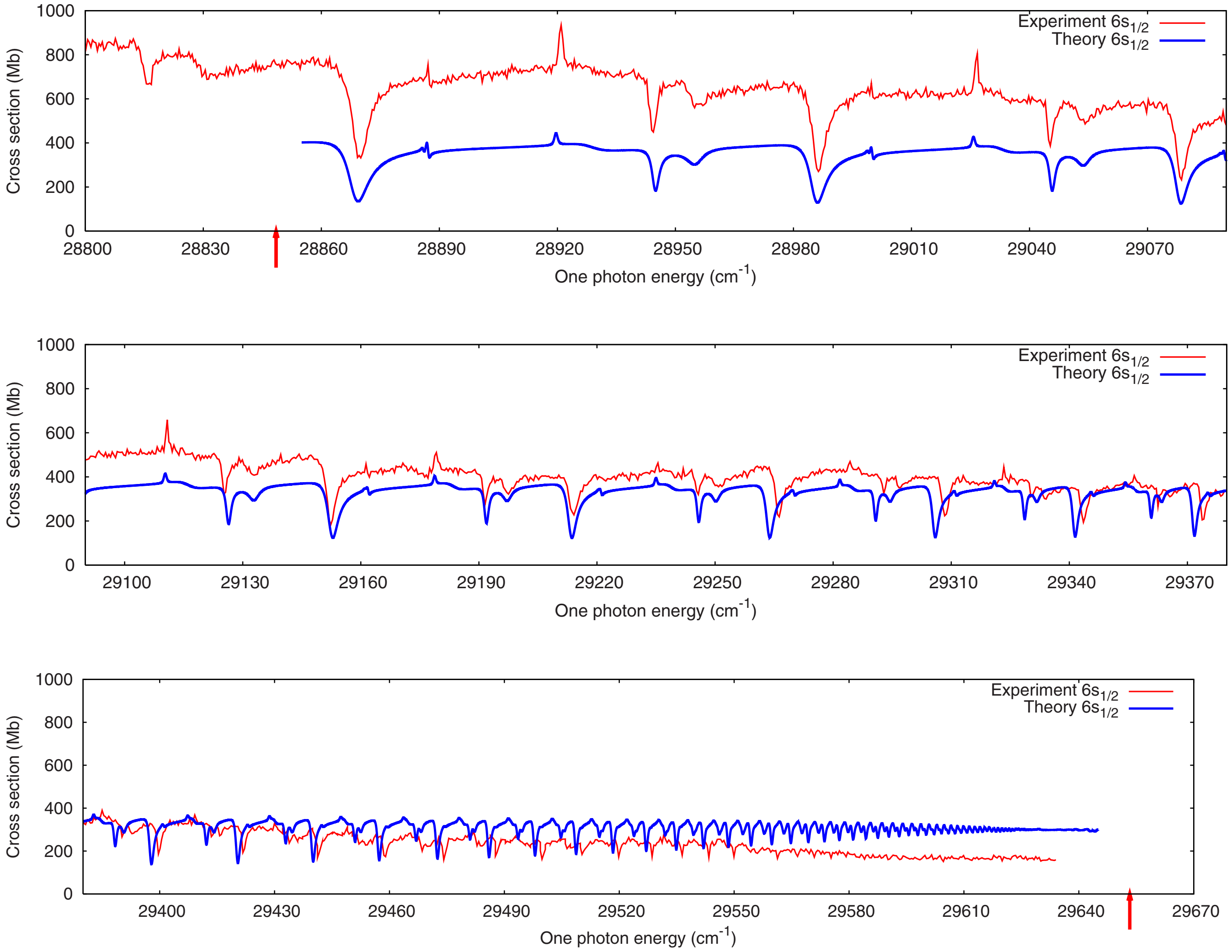

FIG. 4. (Color online) One-photon cross sections: $6s_{1/2}$. The blue (darker gray) line is theory. Experiment is depicted by the red (light gray) line. The $5d_{3/2}$ and $5d_{5/2}$ thresholds are marked with arrows at the low and high end of the spectrum.

priate when ATI is allowed, and the Dalgarno-Lewis method [55] is often applied [47,48].

We treat the continuum intermediate states $|\varepsilon\rangle$ as box states, using a box radius of $60a_0$. We find that this radius is sufficient to converge the results of the calculation. The generalized total cross section for a two-photon transition from a pure initial state can then be represented in terms of T as

$$\sigma^{(2)}(\omega) = 8\pi^3\alpha^2\omega^2\sum_f |T_{f,0}(\omega)|^2, \tag{2}$$

which is defined to have units of (length)^4 (time), such that the probability per unit time, R, of a transition is

$$R = \mathcal{J}^2\sigma^{(2)}, \tag{3}$$

where $\mathcal{J}$ in this equation only is the photon number flux, i.e., the number of photons per unit area per unit time.

The two-photon calculations include closed configurations in which the lowest principal quantum number is no greater than nine, and in which the highest principal quantum number is no greater than 21, 21, or 25 for the initial, intermediate, and final states, respectively. This gives us 1270 configurations for the initial $J=1$ state; 522, 1270, and 1750 configurations for intermediate states with $J=0$, 1, and 2, respectively; and 1584, 2160, and 2304 closed configurations for final states with $J=1$, 2, and 3, respectively.

The larger box radius utilized in the two-photon calculations necessitates that the $5d_{5/2}$ channel is the only one treated as weakly closed, and in contrast to the one-photon calculations we enforce a zero boundary condition at the R-matrix boundary for the higher $6p_{1/2}$ and $6p_{3/2}$ channels.

C. Hyperfine depolarization

As described in Ref. [38], it is necessary to include the effect of hyperfine depolarization of the initially excited $^1P_1$ state. This state is initially excited to the $m_J=0$ sublevel, but the presence of nuclear spin and the associated hyperfine splittings will in general cause the electronic angular momentum to precess about the total angular momentum, populating the $m_J=\pm 1$ sublevels, which process is called hyperfine depolarization [56,57]. Isotopes of barium with nonzero nuclear spin occur with 18% natural abundance and are therefore subject to hyperfine depolarization.

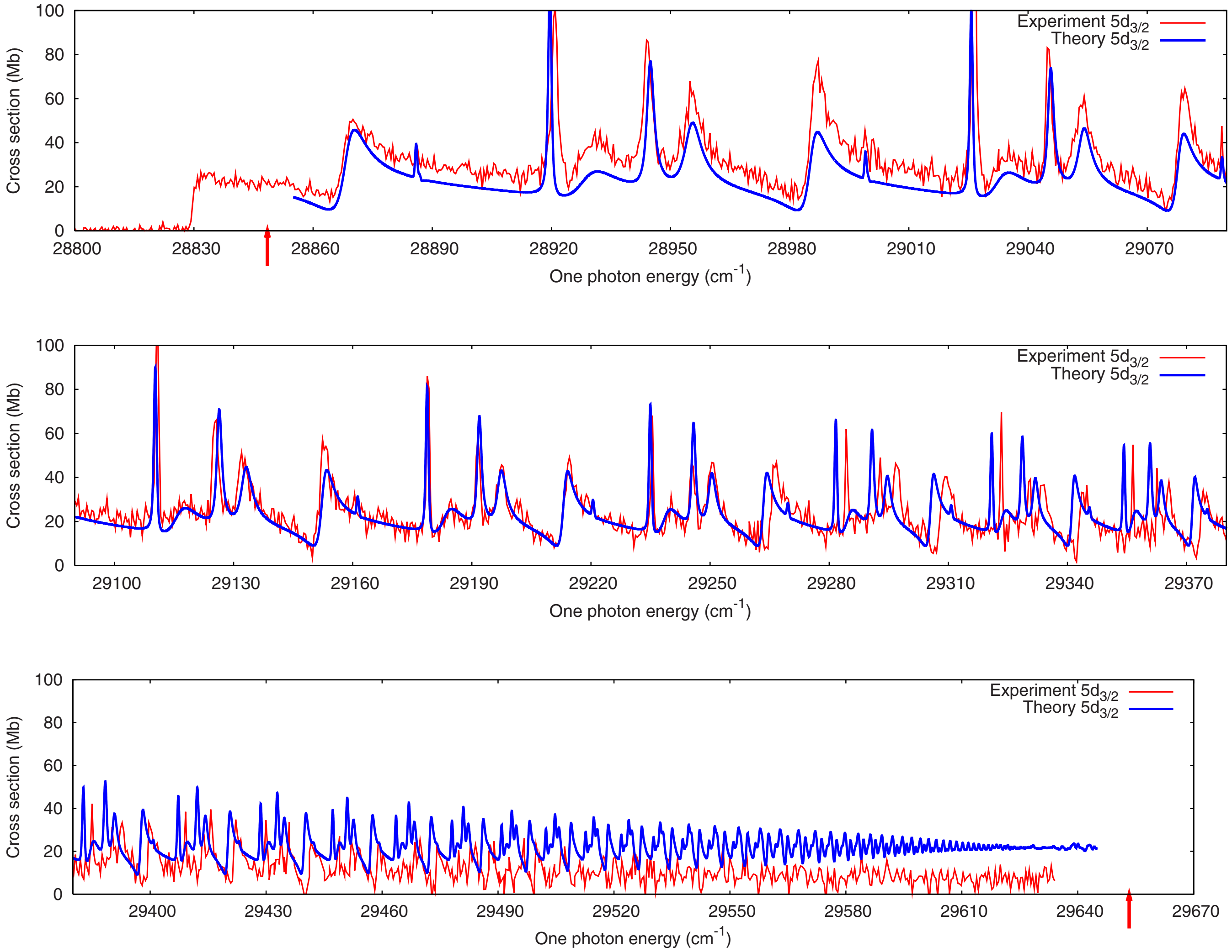

FIG. 5. (Color online) One-photon cross sections: $5d_{3/2}$. The blue (darker gray) line is theory. Experiment is depicted by the red (light gray) line. The $5d_{3/2}$ and $5d_{5/2}$ thresholds are marked with arrows at the low and high end of the spectrum.

In Ref. [38] a parameter g describes the amount of hyperfine depolarization. A value of $g=1.0$ corresponds to no depolarization; the maximum amount of hyperfine depolarization, given a pure initial excitation of the $m_J=0$ sublevel, corresponds to a value of $g=0.896$. We find, however, that the best agreement with experiment is obtained with a value of $g\approx 0.82$. This fact indicates that the initial excitation of the $^1P_1$ state might initially create some population in the $m_J=\pm 1$ sublevels, which in turn could suggest that this transition may be partially saturated in the experiment. This conclusion is consistent with the conditions of the experiment. (The pulse energy, pulse duration and a beam size of $\sim$0.5 mm yield a pulse area of several thousand radians. Thus a perpendicular field component of the ω_0 laser whose relative amplitude was even 10^{-3} would be sufficient to promote a non-negligible population in the $m_J=\pm 1$ sublevels.)

IV. SPECTRA

Figures 4, 5, 7, and 8 show the product-resolved photoionization partial cross sections obtained, in the energy region between the $5d_{3/2}$ and $5d_{5/2}$ thresholds, for one- and two-photon excitation from the $6s6p$ $^1P_1$ state. All the spectra show many final-state autoionizing peaks converging to the $5d_{5/2}$ threshold, modulating a continuum of slowly varying background ionization.

The abscissae in Figs. 4, 5, 7, and 8 are labeled in terms of the energy above the initial $^1P_1$ state, which lies at 18060.261 cm^{-1} above the ground state of the neutral. The $5d_{3/2}$ and $5d_{5/2}$ thresholds are located at red wavelengths of 693.277 and 674.549 nm (whose doubled wavenumbers are at 28848.50 and 29649.46 cm^{-1}), calculated from the ionization threshold energy of 46908.76 cm^{-1} and 47709.72 cm^{-1}, respectively, and the $6s6p$ $^1P_1$ state energy [27]. The threshold for $5d_{3/2}$ can be observed as a sudden drop of the signal, near a red wavelength of 693.7 nm (28830 cm^{-1}), in the one- and two-photon slow electron spectra.

For both spectra, partial cross sections into the slow electron channels are much smaller than for the faster electron channels. In the one-photon spectra, there are many resonance structures with relatively large background ionization; in contrast, the two-photon spectra show more pronounced autoionizing peaks with simpler structures.

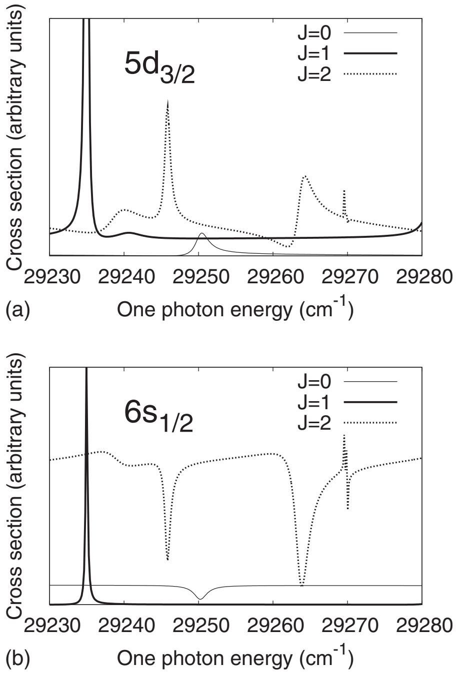

FIG. 6. Zoom of one-photon isotropic (Ref. [38]) cross sections calculated separately for $J=0$, 1, and 2 final states.

Because the experimental data are not absolutely normalized, we have normalized the experiment to theory. In doing so we use the same constant for the fast ($6s_{1/2}$) and slow ($5d_{3/2}$) partial cross sections.

A. One-photon cross sections

Figures 4 and 5 depict the one-photon partial cross section for the $6s_{1/2}$ and $5d_{3/2}$ channels. There are several series of autoionizing resonances visible in these results. These can be identified by referring to Fig. 6, which shows cross sections calculated for one final angular-momentum value J at a time over a small energy range.

Hyperfine depolarization is responsible for the presence of the $J=1$ final-state resonance series, and this series may be used to infer the amount of depolarization present in the experiment. The $J=1$ resonant autoionizing series is prominent in the $5d_{3/2}$ final-state cross section but relatively smaller in the $6s_{1/2}$ cross section.

We find that hyperfine depolarization effects [38] are insufficient to account for the observed magnitude of the $J=1$ resonance series in the $5d_{3/2}$ cross section. The parameter g used in Ref. [38]. indicates the amount of depolarization and for barium has a maximum value of 1.0, corresponding to no depolarization, and a minimum of 0.896, corresponding to maximum hyperfine depolarization. We find that a value of $g=0.82$ produces the best agreement between theory and experiment. Therefore, it seems that there is depolarization in the experiment beyond that describable via the hyperfine depolarization mechanism alone, which might reflect some combination of saturation and/or polarization impurity in the excitation lasers.

B. Two-photon cross sections

Two-photon ionization cross sections are shown in Figs. 7 and 8. The resonance series in the two-photon cross sections are members of one of two previously identified autoionizing series, $5d\ ^2D_{5/2}np_{3/2}$ and $5d\ ^2D_{5/2}nf_{3/2}$ [43]. There is one experimental peak not reproduced by the theory, which lies at a two-photon energy of approximately 28974 cm^{-1} (i.e., a red wavelength of 690.28 nm). This energy corresponds to a one-photon transition to the $6s7p\ ^1P_1$ state, which lies at

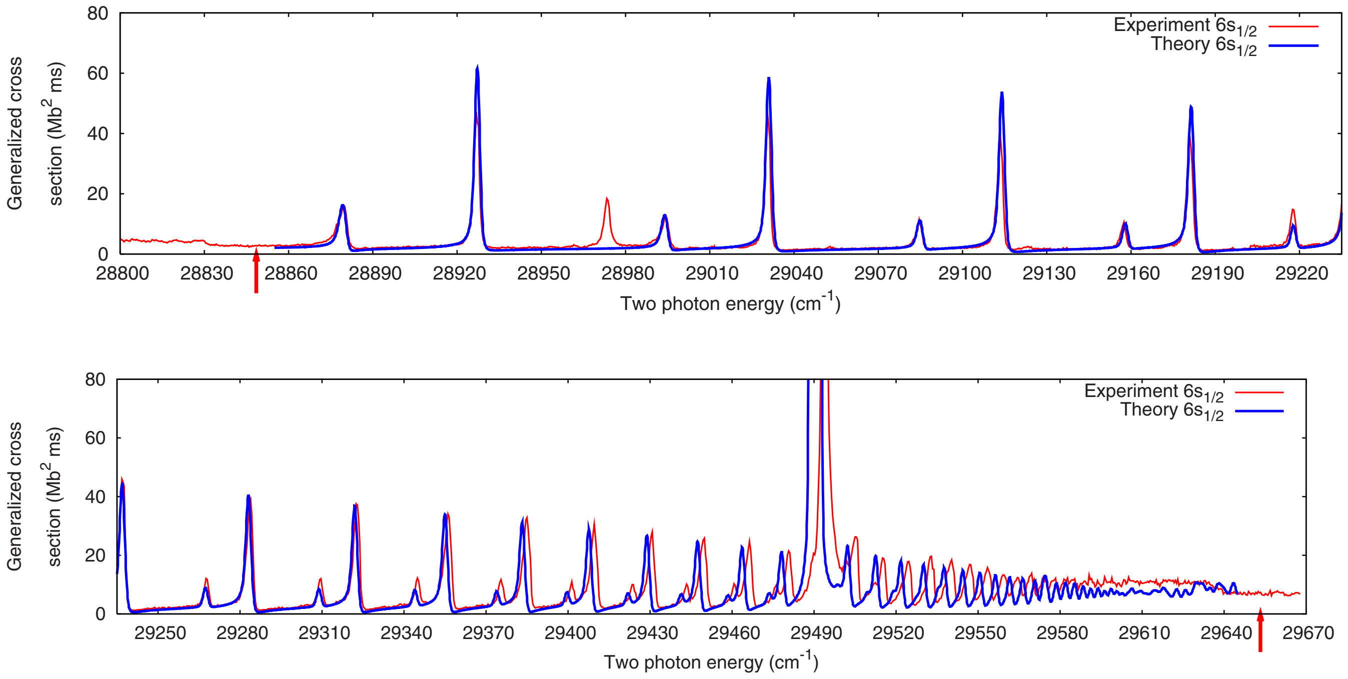

FIG. 7. (Color online) Two-photon generalized cross sections: $6s_{1/2}$. The blue (darker gray) line is theory. Experiment is depicted by the red (light gray) line. The $5d_{3/2}$ and $5d_{5/2}$ thresholds are marked with arrows at the low and high end of the spectrum.

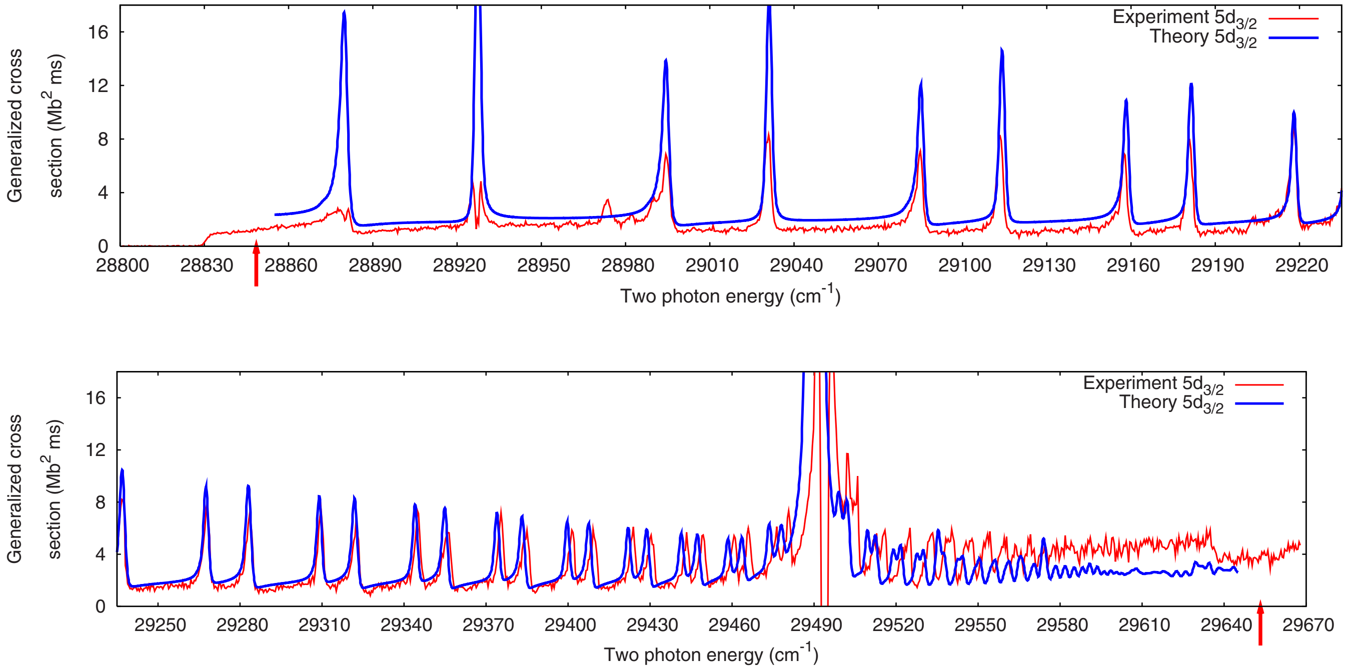

FIG. 8. (Color online) Two-photon generalized cross sections: $5d_{3/2}$. The blue (darker gray) line is theory. Experiment is depicted by the red (light gray) line. The $5d_{3/2}$ and $5d_{5/2}$ thresholds are marked with arrows at the low and high end of the spectrum.

32547.033 cm^{-1} above the ground state, and it therefore seems that this is an intermediate-state resonance reached via a quadrupole transition from the initial state. We use the location of this peak to establish an absolute frequency calibration of our laser scan. This peak in the two-photon spectrum allows us to calibrate our uv wavelengths as well, since these wavelengths are determined through measurements of the wavelength of the red laser beam before we double its frequency using the nonlinear crystal. Therefore, we use this extra peak in the two-photon spectra to calibrate the *absolute* frequency shown in the measured spectra of Figs. 4, 5, 7, and 8.

The strong peak around 678 nm (29489.5 cm^{-1}) in the red (two photon) spectrum is due to the existence of an intermediate-state resonance (554 nm+678 nm) with the $5d7s\ ^3D_1$ state, which lies 32805.169 cm^{-1} above the neutral barium ground state. This intermediate state has total angular-momentum $J=1$ and is therefore excited only to the extent that there is depolarization of the laser-excited $^1P_1$ state (or impurity in the linearly polarized beam). It allows us to obtain an estimate of the amount of depolarization present in the experiment independent of the one-photon results. However, because of the fact that we have only one peak to which to refer, and because the theoretical perturbation-theory results are invalid in the immediate vicinity of the resonance at 29489.5 cm^{-1}, the estimate of depolarization from the two-photon results is less precise than is that from the one-photon results. However, we find that a value of $g=0.82$ does produce better agreement than does the value of $g=0.896$ corresponding to the maximum possible assuming only hyperfine depolarization, corroborating the estimate obtained from the one-photon results that there must be depolarization in the experiment beyond that expected from hyperfine depolarization alone.

We see evidence of the false counting at low electron kinetic energies that was mentioned above, in the slow electron peaks in the red laser (two photon) spectrum in Fig. 7 at 691.4 and 692.6 nm (28927 and 28877 cm^{-1}), causing the double-peak feature at these locations.

We calculate that the ionized electron is mostly p wave, with some f wave, confirming the conclusions based upon photoelectron angular distributions measurements to this effect in Refs. [20,21], as can be seen in Fig. 9. The dominant final-state total angular momentum for the two-photon ionization process is $J=1$.

The dominant intermediate-state angular momentum is $J=1$ for the contribution from hyperfine depolarization, and $J=2$ for the polarized contribution. Of the $J=2$ intermediate virtual states that contribute to the cross section, the dominant one is the $6s6d\ ^1D$ state, at 30236.828 cm^{-1} (corresponding to a 2ω value of 24 354 as plotted in the figures). Also, the $5d7s\ ^3D$ state at 32943.774 cm^{-1} contributes to the cross section at the highest energy range for the $5d_{3/2}$ channel (above the intermediate-state peak).

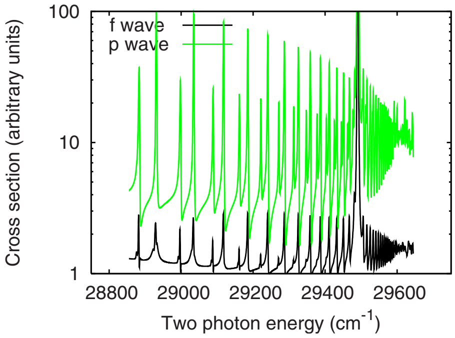

FIG. 9. (Color online) Cross sections (summed for both final electronic state channels) as a function of the outgoing partial wave. The black line is f wave and the green (light gray) line is p wave.

V. CONCLUSIONS

This combined theoretical and experimental study has given a quantitative understanding of the one- and two-photon photoionization spectra of barium, starting from the laser-excited $6s6p\ ^1P^{\circ}$ level. This should now enable a careful study of the phase-dependent interference between one- and two-photon ionization of this barium excited state, and hopefully permit a quantitative test of this interference theory as well as the accuracy of the phases predicted by theory at the level described in the present study.

We thank J. P. D'Incao and S. T. Rittenhouse for helpful discussions. This work was supported in part by the Department of Energy, Office of Science. The material in the experimental section is based upon work supported by the National Science Foundation under Grant No. 0099477.

---

[1] P. Brumer and M. Shapiro, Chem. Phys. Lett. **126**, 541 (1986).

[2] P. Brumer and M. Shapiro, Faraday Discuss. Chem. Soc. **82**, 177 (1986b).

[3] C. Chen, Y.-Y. Yin, and D. S. Elliott, Phys. Rev. Lett. **64**, 507 (1990).

[4] S. M. Park, S.-P. Lu, and R. J. Gordon, J. Chem. Phys. **94**, 8622 (1991).

[5] L. Zhu, V. Kleiman, X. Li, S. Lu, K. Trentelman, and R. Gordon, Science **270**, 77 (1995).

[6] A. Shnitman, I. Sofer, I. Golub, A. Yogev, M. Shapiro, Z. Chen, and P. Brumer, Phys. Rev. Lett. **76**, 2886 (1996).

[7] A. Haché, Y. Kostoulas, R. Atanasov, J. L. P. Hughes, J. E. Sipe, and H. M. van Driel, Phys. Rev. Lett. **78**, 306 (1997).

[8] H. M. van Driel, J. E. Sipe, A. Haché, and R. Atanasov, Phys. Status Solidi B **204**, 3 (1997).

[9] L. Zhu, K. Suto, J. A. Fiss, R. Wada, T. Seideman, and R. J. Gordon, Phys. Rev. Lett. **79**, 4108 (1997).

[10] A. Khachatrian, R. Billoto, L. Zhu, R. Gordon, and T. Seideman, J. Chem. Phys. **116**, 9326 (2002).

[11] J. A. Fiss, L. Zhu, R. J. Gordon, and T. Seideman, Phys. Rev. Lett. **82**, 65 (1999).

[12] P. Lambropoulos and T. Nakajima, Phys. Rev. Lett. **82**, 2266 (1999).

[13] H. Lefebvre-Brion, J. Chem. Phys. **106**, 2544 (1997).

[14] T. Nakajima, J. Zhang, and P. Lambropoulos, J. Phys. B **30**, 1077 (1997).

[15] A. Lyras and H. Bachau, Phys. Rev. A **60**, 4781 (1999).

[16] S. Lee, J. Chem. Phys. **108**, 3903 (1998).

[17] T. Seideman, J. Chem. Phys. **108**, 1915 (1998).

[18] T. Seideman, J. Chem. Phys. **111**, 9168 (1999).

[19] A. Apalategui, A. Saenz, and P. Lambropoulos, Phys. Rev. Lett. **86**, 5454 (2001).

[20] R. Yamazaki and D. S. Elliott, Phys. Rev. Lett. **98**, 053001 (2007).

[21] R. Yamazaki and D. S. Elliott, Phys. Rev. A **76**, 053401 (2007).

[22] H. Feshbach, Ann. Phys. **19**, 287 (1962).

[23] U. Fano, Phys. Rev. **124**, 1866 (1961).

[24] U. Fano and D. Dill, Phys. Rev. A **6**, 185 (1972).

[25] M. D. Lindsay, C.-J. Dai, L.-T. Cai, T. F. Gallagher, F. Robicheaux, and C. H. Greene, Phys. Rev. A **46**, 3789 (1992).

[26] D. Z. Anderson, N. B. Baranova, C. H. Greene, and B. Ya. Zel'dovich, Sov. Phys. JETP **75**, 210 (1992).

[27] H. Karlsson and U. Litzén, Phys. Scr. **60**, 321 (1999).

[28] H. Helm, N. Bjerre, M. J. Dyer, D. L. Huestis, and M. Saeed, Phys. Rev. Lett. **70**, 3221 (1993).

[29] R. Yamazaki and D. S. Elliott, Phys. Rev. A **73**, 023415 (2006).

[30] U. Fano and A. R. P. Rau, *Atomic Collisions and Spectra* (Academic, New York, 1986).

[31] M. J. Seaton, Rep. Prog. Phys. **46**, 167 (1983).

[32] P. Burke and K. A. Berrington, *Atomic and Molecular Processes: An R*-Matrix Approach (Taylor & Francis, London, 1993).

[33] M. Aymar and O. Robaux, J. Phys. B **12**, 531 (1979).

[34] C. H. Greene and L. Kim, Phys. Rev. A **36**, 2706 (1987).

[35] C. H. Greene and C. E. Theodosiou, Phys. Rev. A **42**, 5773 (1990).

[36] M. Aymar, J. Phys. B **23**, 2697 (1990).

[37] C. H. Greene and M. Aymar, Phys. Rev. A **44**, 1773 (1991).

[38] R. P. Wood, C. H. Greene, and D. Armstrong, Phys. Rev. A **47**, 229 (1993).

[39] D. J. Armstrong, R. P. Wood, and C. H. Greene, Phys. Rev. A **47**, 1981 (1993).

[40] D. Armstrong, C. H. Greene, R. P. Wood, and J. Cooper, Phys. Rev. Lett. **70**, 2379 (1993).

[41] R. P. Wood and C. H. Greene, Phys. Rev. A **49**, 1029 (1994).

[42] J.-M. Lecomte, M. Telmini, M. Aymar, and E. Luc-Koenig, J. Phys. B **27**, 667 (1994).

[43] K. Maeda, K. Ueda, M. Aymar, T. Matsui, H. Chiba, and K. Ito, J. Phys. B **33**, 1943 (2000).

[44] M. Aymar, C. H. Greene, and E. Luc-Koenig, Rev. Mod. Phys. **68**, 1015 (1996).

[45] C. H. Greene and L. Kim, Phys. Rev. A **38**, 5953 (1988).

[46] M. Madine and H. W. van der Hart, J. Phys. B **38**, 1895 (2005).

[47] E. Luc-Koenig, A. Lyras, J. M. Lecomte, and M. Aymar, J. Phys. B **30**, 5213 (1997).

[48] F. Robicheaux and B. Gao, Phys. Rev. Lett. **67**, 3066 (1991).

[49] S. Benec'h and H. Bachau, J. Phys. B **37**, 3521 (2004).

[50] R. Santra, K. V. Christ, and C. H. Greene, Phys. Rev. A **69**, 042510 (2004).

[51] S. Cohen, I. Liontos, A. Bolovinos, A. Lyras, S. Benec'h, and H. Bachau, J. Phys. B **39**, 2693 (2006).

[52] E. Luc-Koenig, M. Aymar, M. Millet, J. M. Lecomte, and A. Lyras, Eur. Phys. J. D **10**, 205 (2000).

[53] S. Mengali and R. Moccia, J. Phys. B **29**, 1613 (1996).

[54] E. Cormier and P. Lambropoulos, J. Phys. B **28**, 5043 (1995).

[55] A. Dalgarno and J. T. Lewis, Proc. R. Soc. London, Ser. A **233**, 70 (1955).

[56] U. Fano and J. H. Macek, Rev. Mod. Phys. **45**, 553 (1973).

[57] C. H. Greene and R. N. Zare, Annu. Rev. Phys. Chem. **33**, 119 (1982).